

# Compact [C II] emitters around a C IV absorption complex at redshift 5.7

<https://doi.org/10.1038/s41586-023-05901-3>

Received: 15 June 2022

Accepted: 28 February 2023

Published online: 10 May 2023

 Check for updates

Daichi Kashino<sup>1,2</sup>✉, Simon J. Lilly<sup>3</sup>, Robert A. Simcoe<sup>4</sup>, Rongmon Bordoloi<sup>5</sup>, Ruari Mackenzie<sup>3</sup>, Jorryt Matthee<sup>3</sup> & Anna-Christina Eilers<sup>4</sup>

The physical conditions of the circumgalactic medium are investigated by means of intervening absorption-line systems in the spectrum of background quasi-stellar objects (QSOs) out to the epoch of cosmic reionization<sup>1–4</sup>. A correlation between the ionization state of the absorbing gas and the nature of the nearby galaxies has been suggested by the sources detected in either Ly $\alpha$  or [C II] 158 μm near to, respectively, highly ionized and neutral absorbers<sup>5,6</sup>. This is also probably linked to the global changes in the incidence of absorption systems of different types and the process of cosmic reionization<sup>7–12</sup>. Here we report the detection of two [C II]-emitting galaxies at redshift  $z \approx 5.7$  that are associated with a complex, high-ionization C IV absorption system. These objects are part of an overdensity of galaxies and have compact sizes (<2.4 kpc) and narrow linewidths (full width at half maximum (FWHM)  $\approx 62\text{--}64 \text{ km s}^{-1}$ ). Hydrodynamic simulations predict that similar narrow [C II] emission may arise from the heating of small ( $\lesssim 3$  kpc) clumps of cold neutral medium or a compact photodissociation region<sup>13,14</sup>. The lack of counterparts in the rest-frame ultraviolet (UV) indicates severe obscuration of the sources that are exciting the [C II] emission. These results may suggest a connection between the properties of the [C II] emission, the rare overdensity of galaxies and the unusual high ionization state of the gas in this region.

Two line emitters are detected within a mosaiced submillimetre observation with the Atacama Large Millimeter Array (ALMA) that covers a field of about 23'' (138 physical kpc (pkpc) at  $z = 5.7$ ) in radius centred on the position of QSO J1030+0524 at redshift  $z_{\text{QSO}} = 6.308$ . We interpret these two emission lines to be [C II] 158 μm at redshifts close to that of a complex C IV absorption system with three distinct absorbers at  $z_{\text{abs}} = 5.7246, 5.7411$  and  $5.7443$  found in a deep, high-resolution spectrum of the QSO. These two sources were discovered in blind line searches within a larger datacube that covers a circular survey area of 23'' (138 pkpc at  $z = 5.7$ ) and a total velocity interval  $7,380 \text{ km s}^{-1}$ , corresponding to approximately 76 comoving Mpc. No other notable lines were detected. We estimated the reliability of both these detections to be  $>95\%$ . The probability for these two line sources to be unrelated CO interlopers at low redshifts was calculated to be 1.5% and this possibility is further disfavoured by other ancillary data in this region (see Methods).

The first source, referred to as [C II]1030A, at  $z_{[\text{C II}]} = 5.7354$ , has an impact parameter to the quasar sightline (the transverse separation from the line of sight at the redshift of the intervening system) of 86 pkpc. The second source, [C II]1030B, at  $z_{[\text{C II}]} = 5.7101$ , is at 109 pkpc (Fig. 1a). These sources have peak signal-to-noise ratios (S/N) greater than 6.0 when collapsing the emission-line channels over  $66 \text{ km s}^{-1}$  (Methods). The [C II] moment-0 intensity maps of these [C II] sources are shown in Fig. 1b,c. Notably, these two sources are not spatially resolved under the synthesized FWHM beam size of 0.35'', putting a

strong constraint on the FWHM size of the [C II] sources to be less than 2.4 pkpc. The spectra of these sources are shown in Fig. 2a,b, in comparison with the C IV absorption profiles in the continuum-normalized spectrum of QSO J1030+0524 (Fig. 2c; Methods). These ALMA spectra are extracted within a radius of 0.24'' of the peak position. By fitting a simple Gaussian profile, we estimate the FWHM linewidths to be  $64 \pm 11 \text{ km s}^{-1}$  ([C II]1030A) and  $62 \pm 11 \text{ km s}^{-1}$  (B), and the velocity-integrated [C II] flux densities to be  $0.174 \pm 0.027 \text{ Jy km s}^{-1}$  (A) and  $0.276 \pm 0.044 \text{ Jy km s}^{-1}$  (B) after correcting for the primary beam response (Methods). The two dashed lines represent the four spectral channels, equivalent to a velocity width of  $66 \text{ km s}^{-1}$ , used to create the moment-0 maps. The total [C II] luminosity is  $L_{[\text{C II}]} = (1.61 \pm 0.24) \times 10^8 L_\odot$  and  $(2.21 \pm 0.36) \times 10^8 L_\odot$ , respectively, for [C II]1030A and B. Figure 2d summarizes the kinematic structure of the [C II] sources relative to the absorption systems. [C II]1030A ( $z_{[\text{C II}]} = 5.7354$ ) has a velocity difference of  $\Delta V = +485 \text{ km s}^{-1}$  relative to the stronger absorption system at  $z_{\text{abs}} = 5.7246$ . [C II]1030B ( $z_{[\text{C II}]} = 5.7101$ ) is at  $\Delta V = -645 \text{ km s}^{-1}$ . Note that [C II]1030A has a velocity difference of  $\Delta V = -250 \text{ km s}^{-1}$  relative to its closest (and weakest) absorption system at  $z_{\text{abs}} = 5.7411$ . The ALMA measurements (primary-beam-corrected values) of the [C II] sources are summarized in Table 1.

The impact parameters of these [C II] sources are within the range seen previously for associations between metal absorbers and (non-[C II]) galaxies at lower redshifts<sup>15</sup>. The velocity offsets are also comparable with the velocity dispersion of protoclusters identified at

<sup>1</sup>Institute for Advanced Research, Nagoya University, Nagoya, Japan. <sup>2</sup>Department of Physics, Nagoya University, Nagoya, Japan. <sup>3</sup>Department of Physics, ETH Zürich, Zürich, Switzerland. <sup>4</sup>MIT Kavli Institute for Astrophysics and Space Research, Cambridge, MA, USA. <sup>5</sup>Department of Physics, North Carolina State University, Raleigh, NC, USA. ✉e-mail: kashinod.astro@gmail.com

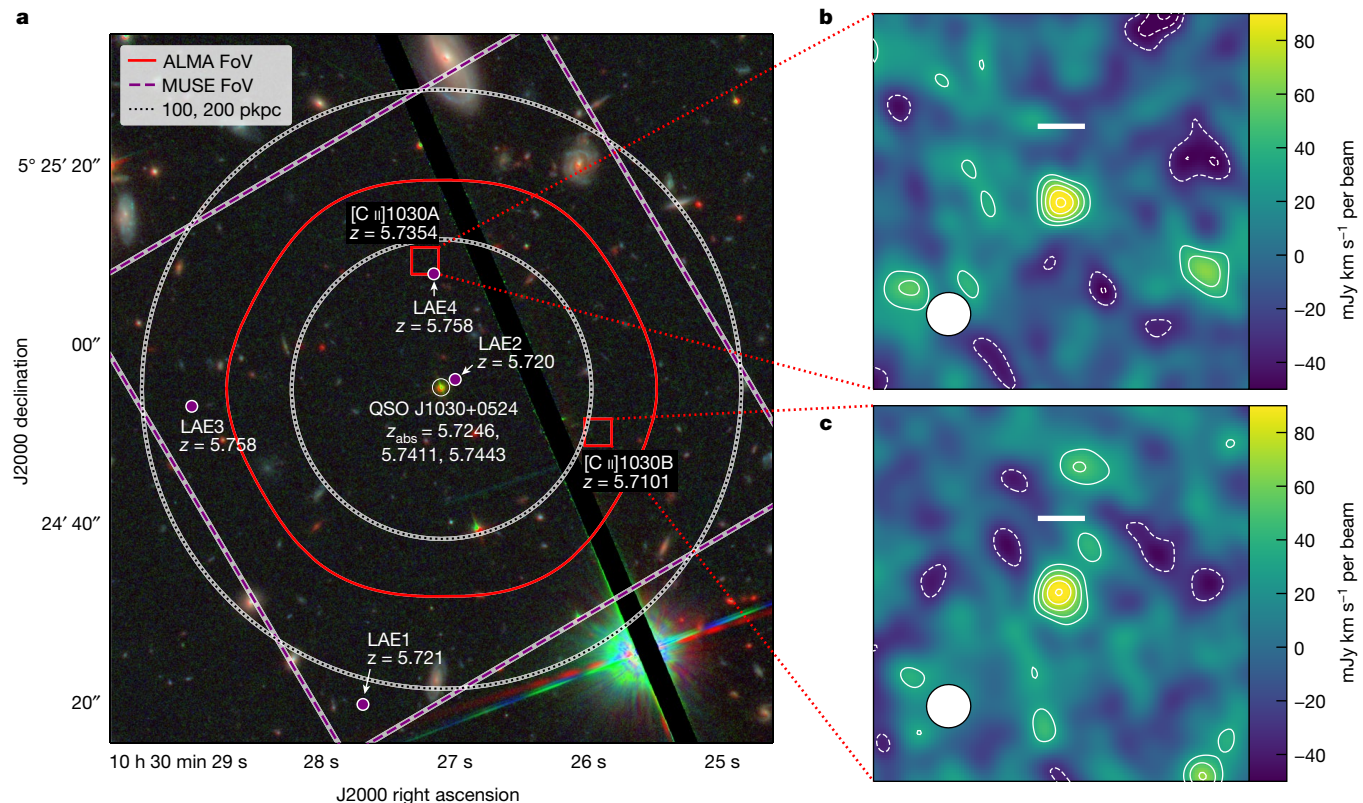


**Fig. 1 | ALMA observations of the two [C II] sources.** **a**, The field of QSO J1030+0524. The background is a composite colour image of the field with the HST images in the F775W, F850LP and F160W bands. The field of view (FoV) of the ALMA observation is marked by the red line. The [C II]-detected sources ([C II]1030A and [C II]1030B) are marked by red squares. The large dotted-line circles denote the radii of 100 pkpc and 200 pkpc from the central QSO. For

comparison, the purple dots indicate the locations of four Ly $\alpha$  emitters (LAE1–LAE4) found in the MUSE datacube whose FoV is marked by the large dashed-purple-line square<sup>5</sup>. **b,c**, [C II] moment-0 maps ( $3'' \times 3''$ ) of [C II]1030A and [C II]1030B, respectively. The solid (dashed) contours mark positive (negative) steps of  $1\sigma$  ( $\approx 0.25$  mJy km s $^{-1}$  per beam) starting at  $2\sigma$  ( $-2\sigma$ ). The sizes of the synthesized beams are indicated at the bottom left. Scale bars, 2 pkpc.

similar high redshifts<sup>16</sup> and for companion [C II] sources ( $\lesssim 100$  pkpc) observed around  $z > 6$  luminous quasars<sup>17</sup>. A similar extent is also found in zoom-in simulations that follow the formation of a massive protocluster at  $z \approx 6$  (ref. 18). All these arguments support a physical connection between the [C II] sources and the C IV absorbing gas through a common membership of some larger structure(s) that may enclose all these systems, rather than the C IV absorption coming from gas falling into or flowing out of these individual sources.

This statement is further strengthened by the locations of the four Lyman- $\alpha$  emitters (LAEs) that have been discovered in this region. Figures 1a and 2d mark these LAEs (purple circles) detected within  $\pm 1,500$  km s $^{-1}$  of the C IV absorbers with the Multi-Unit Spectroscopic Explorer (MUSE) on the Very Large Telescope (VLT)<sup>5</sup>. The two [C II] sources and the four LAEs are all distinct sources. Although one of the LAEs (LAE4;  $z = 5.758$ ) has a small separation of only  $1.7''$  from [C II]1030A (equivalent to 10 pkpc), the redshift difference between these two sources corresponds to more than 1,000 km s $^{-1}$ , suggesting that they are different objects. The typical impact parameter of the galaxies found here, roughly 100 pkpc, is comparable with the size of the most massive halos, of mass  $10^{13} M_{\odot}$ , at this epoch. However, the radial velocity dispersion of all six sources,  $\sigma(v_r) = 830 \pm 270$  km s $^{-1}$ , is larger than expected for such halos (about 200 km s $^{-1}$ ). Therefore, the system is unlikely to be virialized. The discovery of the [C II] sources has further strengthened this hypothesis.

These two sources are both characterized by compact sizes (FWHM diameter  $< 2.4$  pkpc) and narrow [C II] emission-line profiles ( $64 \pm 11$  km s $^{-1}$  and  $62 \pm 11$  km s $^{-1}$ , respectively, for [C II]1030A and B). These properties differ from other high-redshift [C II] emitters reported previously, which generally have a major-axis FWHM of less than 4 pkpc

and a [C II] linewidth FWHM greater than 200 km s $^{-1}$  (refs. 19–22). Hydrodynamic simulations have suggested that the [C II] emission can be dominated by a narrow (FWHM  $< 100$  km s $^{-1}$ ) line produced by molecular clouds and photodissociation regions within a compact region (about 2 pkpc) of a galaxy<sup>14,23</sup> or by small (approximately 2 pkpc) clumps of cold neutral medium that displaced by several pkpc from the main body of a galaxy undergoing intense star formation<sup>13</sup>. Note that the contrast of emission from cold neutral medium clumps may be substantially reduced as the cosmic microwave background radiation increases in temperature with redshift (the cosmic microwave background is at 18.5 K at  $z = 5.7$ ) so as to be similar to the excitation temperature of the emission<sup>14</sup>.

In both cases, the [C II] emission is excited by far-ultraviolet (FUV) radiation from continuing star formation. Using an empirical relation between  $L_{[C\,II]}$  and star formation rate (SFR), the measured  $L_{[C\,II]}$  would correspond to a [C II]-based SFR of  $SFR_{[C\,II]} = 14 M_{\odot} \text{ year}^{-1}$  ([C II]1030A) and  $19 M_{\odot} \text{ year}^{-1}$  (B), respectively, with an expected uncertainty of a factor of 2 owing to the scatter<sup>24,25</sup>. Theoretical studies predict consistent values for gas clouds of solar metallicity<sup>14</sup>. These sources were not detected in a rest-frame far-infrared (FIR) continuum, yielding only a loose  $2\sigma$  upper limit to the infrared-based SFR of around  $30 M_{\odot} \text{ year}^{-1}$ , which is still consistent with the [C II]-inferred SFR.

For our claimed [C II] sources, no notable counterparts have been found so far either in the Ly $\alpha$  emission line or in the rest-frame FUV continuum, despite the availability of deep Hubble Space Telescope (HST) images and the MUSE datacube. The lack of detection in an HST image (approximately 9,000 Å observed or about 1,350 Å in the rest frame) gives a  $2\sigma$  upper limit of about 59 nJy, which corresponds at this redshift to a FUV-based SFR of about  $2 M_{\odot} \text{ year}^{-1}$  (Methods), considerably lower

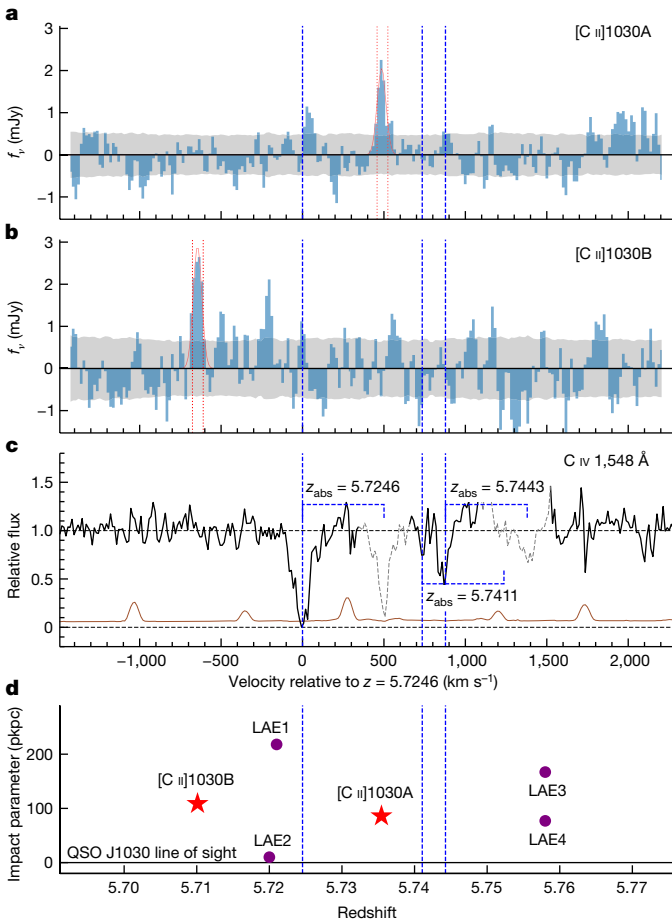


**Fig. 2 | Emission and absorptions spectra of the [C II] sources and QSO J1030+0524.** **a,b**, ALMA spectra of the [C II] 158  $\mu\text{m}$  emission of the [C II]1030A and B sources, respectively. The grey-shaded region indicates the  $1\sigma$  noise. The solid red line shows a single-Gaussian model fit to the data. The dotted red vertical lines mark the channel intervals that were collapsed to generate the [C II] moment-0 maps. The dashed blue vertical lines indicate the location of three absorbers. The origin of the velocity scale was chosen to correspond to the strongest C IV absorption system at  $z_{\text{abs}} = 5.7246$ . **c**, Absorption profiles of the C IV doublet in the continuum-normalized spectrum of QSO J1030+0524. The C IV doublet lines in the same system are connected. The velocity scale is applicable to the bluer line (rest frame 1,548  $\text{\AA}$ ) of the doublet. The dashed-grey regions in the spectrum indicate the redder (1,550  $\text{\AA}$ ) line. The brown line indicates the  $1\sigma$  noise spectrum. **d**, Impact parameter versus redshift and radial velocity relative to the strongest C IV absorber at  $z_{\text{abs}} = 5.7246$ . They  $y = 0$  line corresponds to the QSO sightline. The [C II] sources are highlighted by red stars and the four MUSE LAEs are represented by purple dots.

than the [C II]-based SFRs. This therefore suggests that the FUV emission from SFR at the required levels must have been severely attenuated by dust, which would also explain the absence of Ly $\alpha$ .

The absence of detectable FUV emission is also in some tension with the ‘normal’ [C II] sources that have been detected at similar redshifts, which are usually detected in rest-frame UV and Ly $\alpha$  emission<sup>26,27</sup>, with typical UV obscuration fractions of around 40% (ref. 28). A few other reports of narrow ( $\text{FWHM} = 50–90 \text{ km s}^{-1}$ ) [C II] sources at  $z > 6$  have come from following up sources that had already been detected in Ly $\alpha$  and the FUV<sup>29,30</sup>. This difference with the sources claimed here may be partially explained by the difference in observing strategy: our own study was based on a blind search as against follow-up observations of previously detected FUV sources. However, heavy obscuration may be at odds with the unusual spatial compactness and narrow spectral width of the [C II] sources, which suggest that they are unlikely to

**Table 1 | ALMA measurements for the two [C II] sources**

	[C II]1030A	[C II]1030B
J2000 right ascension	10 h 30 min 27.215 s	10 h 30 min 25.921 s
J2000 declination	+05° 25' 09.36"	+05° 24' 50.20"
Impact parameter (pkpc)	86	109
Redshift	5.7354	5.7101
$\Delta V$ relative to $z_{\text{abs}}$ = 5.7246 ( $\text{km s}^{-1}$ )	+485	-645
$\Delta V$ relative to $z_{\text{abs}}$ = 5.7443 ( $\text{km s}^{-1}$ )	-392	-1,518
$\Delta V$ relative to $z_{\text{abs}}$ = 5.7411 ( $\text{km s}^{-1}$ )	-250	-1,377
FWHM spatial size (pkpc)	<2.4	<2.4
[C II] flux ( $\text{Jy km s}^{-1}$ )	$0.174 \pm 0.027$	$0.276 \pm 0.044$
FWHM linewidth ( $\text{km s}^{-1}$ )	$64 \pm 11$	$62 \pm 11$
[C II] luminosity ( $10^8 L_{\odot}$ )	$1.61 \pm 0.24$	$2.21 \pm 0.36$

The impact parameter is the transverse separation from the QSO J1030+0524 sightline in pkpc and  $\Delta V$  is the velocity shift relative to each of the three discrete C IV absorption components. The [C II] flux and luminosity are corrected for the primary beam response.

be mature massive systems, which are observed as FIR-bright dusty star-forming galaxies at lower redshifts. Rather, they may represent a different population of galaxies specific to the high-redshift universe. On the other hand, simulations show that selective attenuation by dense dust clouds that embed young stellar clusters may lead to absorption of most of the UV luminosity<sup>31</sup>.

We cannot therefore yet make a conclusive statement about the nature of these [C II]-emitting sources. The threefold rarity of simultaneously having (1) these unusual [C II] sources, (2) a strong over-density of galaxies and (3) the rich high-ionization C IV absorption system (rare at these redshifts), however, suggests that there may be some connection between the observed [C II] properties and the unusual high-ionization conditions that are seen in this particular region, which we are observing at the time that the cosmic reionization of the Universe was approaching completion. Addressing this question will require us to bridge the gap between the rest-frame FUV and FIR views of the high-redshift universe to make known the stellar content and the star formation at wavelengths that are much less affected by dust. Deep near-infrared observations with the James Webb Space Telescope will soon allow us to clarify the origin of these unusual [C II] lines and the links between different physical processes occurring within this extreme environment during the end stages of cosmic reionization.

## Online content

Any methods, additional references, Nature Portfolio reporting summaries, source data, extended data, supplementary information, acknowledgements, peer review information; details of author contributions and competing interests; and statements of data and code availability are available at <https://doi.org/10.1038/s41586-023-05901-3>.

- Simcoe, R. A., Sargent, W. L. W., Rauch, M. & Becker, G. Observations of chemically enriched QSO absorbers near  $z=2.3$  galaxies: galaxy formation feedback signatures in the intergalactic medium. *Astrophys. J.* **637**, 648–668 (2006).
- Prochaska, J. X. et al. The UCSD/Keck damped Ly $\alpha$  abundance database: a decade of high-resolution spectroscopy. *Astrophys. J. Suppl. Ser.* **171**, 29–60 (2007).
- Fox, A. J., Ledoux, C., Petitjean, P. & Srianand, R. C IV absorption in damped and sub-damped Lyman- $\alpha$  systems. Correlations with metallicity and implications for galactic winds at  $z=2$ . *Astron. Astrophys.* **473**, 791–803 (2007).
- Bordoloi, R. et al. Resolving the H I in damped Lyman  $\alpha$  systems that power star formation. *Nature* **606**, 59–63 (2022).
- Díaz, C. G. et al. Faint LAEs near  $z > 4.7$  C IV absorbers revealed by MUSE. *Mon. Not. R. Astron. Soc.* **502**, 2645–2663 (2021).
- Wu, Y. et al. A [C II] 158  $\mu\text{m}$  emitter associated with an O I absorber at the end of the reionization epoch. *Nat. Astron.* **5**, 1110–1117 (2021).
- Becker, G. D., Sargent, W. L. W., Rauch, M. & Simcoe, R. A. Discovery of excess O I absorption toward the  $z=6.42$  QSO SDSS J1148+5251. *Astrophys. J.* **640**, 69–80 (2006).

8. Simcoe, R. A. et al. Constraints on the universal C IV mass density at  $z \sim 6$  from early infrared spectra obtained with the Magellan FIRE spectrograph. *Astrophys. J.* **743**, 21 (2011).
9. Chen, S.-F. S. et al. Mg II absorption at  $2 < z < 7$  with Magellan/Fire. III. Full statistics of absorption toward 100 high-redshift QSOs. *Astrophys. J.* **850**, 188 (2017).
10. Codoreanu, A. et al. The CGM and IGM at  $z \sim 5$ : metal budget and physical connection. *Mon. Not. R. Astron. Soc.* **481**, 4940–4959 (2018).
11. Cooper, T. J. et al. Heavy element absorption systems at  $5.0 < z < 6.8$ : metal-poor neutral gas and a diminishing signature of highly ionized circumgalactic matter. *Astrophys. J.* **882**, 77 (2019).
12. Becker, G. D. et al. The evolution of O I over  $3.2 < z < 6.5$ : reionization of the circumgalactic medium. *Astrophys. J.* **883**, 163 (2019).
13. Vallini, L., Gallerani, S., Ferrara, A. & Baek, S. Far-infrared line emission from high-redshift galaxies. *Mon. Not. R. Astron. Soc.* **433**, 1567–1572 (2013).
14. Vallini, L., Gallerani, S., Ferrara, A., Pallottini, A. & Yue, B. On the [CII]-SFR relation in high redshift galaxies. *Astrophys. J.* **813**, 36 (2015).
15. Dutta, R. et al. Metal-enriched halo gas across galaxy overdensities over the last 10 billion years. *Mon. Not. R. Astron. Soc.* **508**, 4573–4599 (2021).
16. Toshikawa, J. et al. Discovery of protoclusters at  $z \sim 3.7$  and 4.9: embedded in primordial superclusters. *Astrophys. J.* **888**, 89 (2020).
17. Venemans, B. P. et al. Kiloparsec-scale ALMA imaging of [C II] and dust continuum emission of 27 quasar host galaxies at  $z \sim 6$ . *Astrophys. J.* **904**, 130 (2020).
18. Zana, T. et al. Enhanced star formation in  $z \sim 6$  quasar companions. *Mon. Not. R. Astron. Soc.* **513**, 2118–2135 (2022).
19. Aravena, M. et al. The ALMA Spectroscopic Survey in the Hubble Ultra Deep Field: search for [C II] line and dust emission in  $6 < z < 8$  galaxies. *Astrophys. J.* **833**, 71 (2016).
20. Neeleman, M. et al. [C II] 158- $\mu\text{m}$  emission from the host galaxies of damped Lyman-alpha systems. *Science* **355**, 1285–1288 (2017).
21. Fujimoto, S. et al. The ALPINE-ALMA [C II] survey: size of individual star-forming galaxies at  $z = 4\text{--}6$  and their extended halo structure. *Astrophys. J.* **900**, 1 (2020).
22. Fudamoto, Y. et al. The ALMA REBELS survey: average [C II] 158  $\mu\text{m}$  sizes of star-forming galaxies from  $z \sim 7$  to  $z \sim 4$ . *Astrophys. J.* **934**, 144 (2022).
23. Olsen, K. P. et al. Simulator of Galaxy Millimeter/Submillimeter Emission (SiGAME): The [C II]-SFR relationship of massive  $z = 2$  main sequence galaxies. *Astrophys. J.* **814**, 76 (2015).
24. De Looze, I. et al. The applicability of far-infrared fine-structure lines as star formation rate tracers over wide ranges of metallicities and galaxy types. *Astron. Astrophys.* **568**, A62 (2014).
25. Schaerer, D. et al. The ALPINE-ALMA [C II] survey. Little to no evolution in the [C II]-SFR relation over the last 13 Gyr. *Astron. Astrophys.* **643**, A3 (2020).
26. Carniani, S. et al. Kiloparsec-scale gaseous clumps and star formation at  $z = 5\text{--}7$ . *Mon. Not. R. Astron. Soc.* **478**, 1170–1184 (2018).
27. Le Fèvre, O. et al. The ALPINE-ALMA [CII] survey. Survey strategy, observations, and sample properties of 118 star-forming galaxies at  $4 < z < 6$ . *Astron. Astrophys.* **643**, A1 (2020).
28. Fudamoto, Y. et al. The ALPINE-ALMA [CII] survey. Dust attenuation properties and obscured star formation at  $z \sim 4.4\text{--}5.8$ . *Astron. Astrophys.* **643**, A4 (2020).
29. Pentericci, L. et al. Tracing the reionization epoch with ALMA: [C II] emission in  $z \sim 7$  galaxies. *Astrophys. J. Lett.* **829**, L11 (2016).
30. Bradač, M. et al. ALMA [C II] 158  $\mu\text{m}$  detection of a redshift 7 lensed galaxy behind RX J1347.1–1145. *Astrophys. J. Lett.* **836**, L2 (2017).
31. Behrens, C., Pallottini, A., Ferrara, A., Gallerani, S. & Vallini, L. Dusty galaxies in the Epoch of Reionization: simulations. *Mon. Not. R. Astron. Soc.* **477**, 552–565 (2018).

**Publisher's note** Springer Nature remains neutral with regard to jurisdictional claims in published maps and institutional affiliations.

Springer Nature or its licensor (e.g. a society or other partner) holds exclusive rights to this article under a publishing agreement with the author(s) or other rightsholder(s); author self-archiving of the accepted manuscript version of this article is solely governed by the terms of such publishing agreement and applicable law.

© The Author(s), under exclusive licence to Springer Nature Limited 2023

## Methods

### Cosmology

Throughout this paper, we adopted a flat  $\Lambda$  cold dark matter cosmology with  $\Omega_\Lambda = 0.69$ ,  $\Omega_M = 0.31$  and  $H_0 = 67.7 \text{ km s}^{-1} \text{ Mpc}^{-1}$  (ref. 32) when calculating physical parameters.

### ALMA observations and data reduction

The ALMA observations reported here were carried out in September 2018 (programme ID 2017.1.00621.S) with the array in a configuration of 43 12-m antennas with baselines from 15 to 1,397 m. The primary beam of the 12-m ALMA antennas is approximately 45" in diameter at about 260 GHz. The dataset used in this study covers a mosaic of seven offset but overlapping pointings that together cover a roughly circular field of approximately 0.46 arcmin<sup>2</sup> centred on the optical coordinate of the background QSO J1030+0524 (10 h 30 min 27.092 s, +05° 24' 55.02"; ref. 33), with 41 min of total on-source integration. Extended Data Fig. 1 shows the mosaiced field coverage, which is approximately a circular region of 23" in radius, and the resulting antenna responses, which are 67% and 47%, respectively, at the positions of [C II]1030A and [C II]1030B.

The datacubes are generated from four spectral windows (SPWs), each of which has a bandwidth of about 1.875 GHz. Of these, two SPWs are adjusted to cover the three absorbers at  $z_{\text{abs}} = 5.7246$ , 5.7411 and 5.7443 in the [C II] 158 μm emission line, respectively, with a minimum overlap at 282.3 GHz to yield a continuous frequency coverage of 280.5–284.0 GHz. The other two SPWs cover other separate frequency ranges around 294 GHz, at which there is no corresponding absorption system seen in the quasar spectrum. Each SPW was divided into 128 channels, each with a width of 15.6 MHz (16.6 km s<sup>-1</sup>), and the instrumental velocity dispersion corresponds to two channels (33 km s<sup>-1</sup>).

The ALMA data were processed using the CASA<sup>34</sup> pipeline for ALMA (version 5.4), using the standard calibration procedure. The final datacubes and the continuum images were obtained using the CASA tclean task with natural weighting to maximize sensitivity. In doing so, we adopted uv taper (a Gaussian taper on the weights of the  $uv$  data) of 0 × 220 mas and a position angle of 119° to circularize the synthesized beam as much as possible. The resulting beam is 0.35" in FWHM diameter. The continuum image that collapses all four SPWs has a 1 $\sigma$  sensitivity of 31 μJy per beam. For the moment-0 [C II] maps, the four channels (62.5 MHz; approximately 66 km s<sup>-1</sup>) that cover the emission line were collapsed, resulting in a 1 $\sigma$  sensitivity of 4.1 (4.2) mJy km s<sup>-1</sup> per beam at the observed frequency of [C II]1030A ([C II]1030B).

### Blind line search

We used the findclumps algorithm<sup>35</sup>, implemented in the interferopy package for Python<sup>36</sup>, for our blind search for emission-line candidates. Briefly, findclumps performs a top-hat convolution to a datacube to generate a set of collapsed images and searches for peaks exceeding a certain S/N threshold. Clumps that are detected with small offsets in spatial position and frequency are cropped as duplicates, keeping the one with the highest S/N in the final catalogue. We ran the line search with frequency window sizes from 4 to 17 channels (corresponding to about 66–282 km s<sup>-1</sup>) and adopted the offset thresholds of 1" and 280 MHz (300 km s<sup>-1</sup>) for cropping duplicates.

To assess the significance of the detections, we performed the same line search for (unphysical) negative peaks and computed the fidelity of the detections, which represents the probability that a positive line detection at a given S/N is real, following the methods in the literature<sup>35</sup>. Extended Data Fig. 2 shows the number of positive and negative peak detections (upper panels) and the fidelity (lower panels) as a function of S/N. Expressing the fidelity with an error function, we found that 95% fidelity is reached as  $S/N = 5.8$ –6.2, with only small variations between the SPWs. We selected the two claimed [C II] sources ([C II]1030A and B), detected in four-channel collapsed images of two SPWs, as the only

sources that have  $>6\sigma$  significance and found that there are no spurious negative signals at this 6.0 $\sigma$  level of significance. The fidelities of the two [C II] sources were computed to be 96% (A) and 99% (B), respectively.

For each of the three absorption systems, a velocity interval of ±700 km s<sup>-1</sup> was taken as the relevant velocity range within which a source could be considered to be associated with the absorber. This yielded a contiguous velocity interval of 2,280 km s<sup>-1</sup>, from −700 km s<sup>-1</sup> of the lower- $z$  absorber's redshift ( $z_{\text{abs}} = 5.7246$ ) to +700 km s<sup>-1</sup> of the higher- $z$  absorber's redshift ( $z_{\text{abs}} = 5.7443$ ), which cover all of the two [C II] sources and four LAEs detected in the MUSE datacube. The small chance that the two most substantial peaks, if actually spurious, both lie within this physically notable region of association boosts the fidelity values of the claimed [C II] detections to >99.9%.

### Reliability check of the detections

We further examined the reliability of the two claimed sources by analysing independent subsets of the data. We processed separately the two independent XX and YY polarization correlations. The [C II] intensity maps were generated from the same emission-line channels and the one-dimensional spectra were extracted from the same spaxels as the full analysis. As shown in Extended Data Fig. 3, the line emission is always detected with consistent observed fluxes at 4.2–4.7 $\sigma$  at the expected spatial position (within <0.2") and at the expected frequency in each of the two independent datasets.

Because the ALMA observations were in the form of a mosaic of seven offset but overlapping pointings, both the claimed sources in fact appear (at a different location relative to the pointing centre) in two independent pointings (Fig. 1), and these pointings could therefore be reduced separately. The moment-0 maps and the spectra, created in the same way as above, are shown in Extended Data Fig. 3. The claimed sources were detected with consistent fluxes at 3.4–5.3 $\sigma$ .

Finally, a similar test was also carried out using a temporal split of the data stream into two equal segments. These two datasets may not strictly be independent because the two observations exposures were made serially without changes in the instrumental setups but serve as a check for whether the signals come from random noise or not: it should be extremely rare that spurious sources owing to random noise are detected consistently in two different exposures. Again, the line emission is consistently detected at the same spatial positions and at the expected frequencies in both the first and second halves of the data, at S/N between 3.9 and 4.9 $\sigma$ .

These tests all convincingly indicate that the detected lines are plausibly real signals from astronomical sources and not random noise or other spurious signals.

### Line identification

We now address the question of whether the line emission is indeed the [C II] 158 μm emission line at the  $z \approx 5.7$  redshift of the C IV absorption system or some other transition at lower redshift produced by unrelated foreground objects (background sources can be safely neglected).

The most likely low-redshift interlopers would be CO(3–2) (at  $z \approx 0.22$ ) or higher-J CO emission ( $z \approx 0.63$ –2.3). Using published CO luminosity functions for the redshift range between 0 and 6 (ref. 37), we estimated that the expected number of CO sources within the whole datacube should be approximately 0.4 sources. In doing so, we considered CO transitions up to  $J = 8$ –7 and used the published Schechter luminosity function parameters derived for each CO transition at the closest redshift. The luminosity function of CO(6–5) at  $z = 2$  was also adopted for CO(7–6) and CO(8–7), as no measurement is provided for these highest transitions. We then considered the expected number of CO sources that should be detected, at a line flux brighter than or equal to the observed flux of the (fainter) [C II]1030A and within the circular survey volume of radius 23" and the frequency (redshift) interval corresponding to the whole ALMA datacube composed of four SPWs. The results are summarized in Extended Data Table 1.

# Article

The chance of finding two unrelated CO sources within the velocity range of interest (across 2,280 km s<sup>-1</sup> around the absorption systems; see above) is therefore on the order  $(0.4 \times 2,280/7,380)^2 \approx 1.5\%$ , which we consider to be very unlikely. Even if we ignore the expected number of CO sources and consider only our observed number of two detected sources within the datacube, the chance that two unrelated emission lines are both found within the limited velocity range of interest is still  $(2,280/7,380)^2 \approx 9.5\%$ . These probabilities therefore suggest that the two emission lines are indeed [C II] emission associated to this redshift range.

Non-detection of both sources in available deep HST images at about 9,000 Å (see below) also argues against any interpretation that places these sources at low redshift ( $z \lesssim 2$ ). This is because, in that case, their stellar continuum should be detectable. The non-detection is consistent with their lying at high redshift ( $z \gtrsim 5$ ) if their FUV and Ly $\alpha$  emission is intrinsically faint or obscured by dust. We therefore identify these two emission-line signals as [C II] emission at  $z \approx 5.7$ .

## The properties of the [C II] sources

We measured the line properties by fitting a simple Gaussian profile to the observed one-dimensional spectra extracted from the spaxels enclosed within 0.24'' of the peak position of the [C II] sources. The velocity-integrated [C II] line flux is measured to be  $0.174 \pm 0.027$  Jy km s<sup>-1</sup> ([C II]1030A) and  $0.276 \pm 0.044$  Jy km s<sup>-1</sup> (B), respectively, with the FWHM linewidths  $64 \pm 11$  km s<sup>-1</sup> ([C II]1030A) and  $62 \pm 11$  km s<sup>-1</sup> (B). These fluxes are the values after correction for the primary beam response (67% and 47% at the positions of [C II]1030A and B, respectively) and for the approximately 20% loss falling outside the aperture of 0.24'' in radius for extracting the spectra.

The corresponding [C II] luminosities are  $L_{[C\,II]} = (1.61 \pm 0.24) \times 10^8 L_\odot$  and  $(2.21 \pm 0.36) \times 10^8 L_\odot$ , respectively, for [C II]1030A and B. An empirical conversion relation of  $\log_{10}(\text{SFR}/(M_\odot \text{ year}^{-1})) = -7.06 + 1.0 \log_{10}(L_{[C\,II]}/L_\odot)$  yields a [C II]-based SFR of  $\text{SFR}_{[C\,II]} = 14 M_\odot \text{ year}^{-1}$  ([C II]1030A) and  $19 M_\odot \text{ year}^{-1}$  (B), respectively, with 0.3 dex uncertainty<sup>24</sup>. Although more recent studies inferred closely consistent conversion relations using high-redshift [C II] sources<sup>25</sup>, the [C II] luminosity at fixed SFR probably decreases when the metallicity is low ( $Z < 0.1\text{--}0.2 Z_\odot$ ; refs. 14,30). For a lower metallicity, the [C II]-based SFR would be even higher and thus requires even more dust obscuration, which is in turn at odds with the low metallicity. Therefore, these [C II] sources are probably as metal-rich as the levels of normal [C II] sources detected at similar redshifts<sup>25,38</sup>.

The ALMA datacubes cover the rest-frame FIR continuum at 1,900 GHz that traces the dust emission. The continuum maps of the sources are shown in Extended Data Fig. 4. We found no detection of the continuum at the positions of the [C II] sources and inferred a  $2\sigma$  upper limit of 106 μJy ([C II]1030A) and 158 μJy (B). To convert this continuum flux to a total infrared luminosity ( $L_{\text{IR}}$ ; 8–1,000 μm), we adopted a conversion factor of  $\nu L_\nu / L_{\text{IR}} = 0.13$  ( $\nu = 1,900$  GHz) that was inferred using a template of the infrared spectral energy distribution of  $z \approx 4$  galaxies<sup>39</sup>. The template is consistent with a modified black-body ( $Sv \approx v^\beta / (\exp(h\nu/kT_{\text{dust}}) - 1)$ ) with a fixed index  $\beta = 1.8$  and dust temperature  $T_{\text{dust}} = 41$  K. This conversion resulted in a  $2\sigma$  upper limit of  $L_{\text{IR}} = 2.3 \times 10^{11} L_\odot$  (A) and  $3.3 \times 10^{11} L_\odot$  (B). Finally, we converted the  $L_{\text{IR}}$  to obscured SFR by adopting the relation ( $\text{SFR}_{\text{IR}} (M_\odot \text{ year}^{-1}) = 1.01 \times 10^{-10} L_{\text{IR}} (L_\odot)$ )<sup>40</sup> converted to an initial mass function<sup>41</sup> and obtained  $\text{SFR}_{\text{IR}} < 23 M_\odot \text{ year}^{-1}$  (A) and  $< 34 M_\odot \text{ year}^{-1}$  (B) at  $2\sigma$ . The  $2\sigma$  lower limits of the  $L_{[C\,II]}/L_{\text{IR}}$  ratio,  $> 7 \times 10^{-4}$ , is consistent with the observed values at similar redshifts<sup>25</sup>, with no evidence of the so-called [C II] deficit.

## Measurements of the absorption systems towards QSO J1030+0524

Our analysis uses revised measurements of the absorption systems at  $z \approx 5.7$  towards QSO J1030+0524, using improved spectra obtained with both VLT/XShooter<sup>42</sup> and the Folded-port InfraRed Echelle (FIRE) on Magellan<sup>43</sup>. Archival XShooter data (acquired under European Southern Observatory (ESO) programmes 084.A-0360(A), 086.A-0162(A),

086.A-0574(A) and 087.A-0607(A)) were retrieved from the ESO Science Archive Facility and reduced using the Pypelt spectroscopic reduction pipeline<sup>44</sup>. The XShooter exposures from different programmes were carefully and individually corrected for telluric absorption using numerical atmospheric models and then optimally combined to maximize S/N. All exposures were obtained with a 0.9'' slit, resulting in spectral resolution  $\lambda/\Delta\lambda = 5,300$ . FIRE exposures were acquired in April 2011 and reduced using the FIREHOSE pipeline<sup>45</sup>. All data used a 0.6'' slit for spectral resolution  $\lambda/\Delta\lambda = 6,000$ . The FIRE spectra were corrected for telluric absorption using observations of AOV standards and a modified version of the xtelcor package<sup>46,47</sup>.

Because the absorption data span three instrument configurations (XShooter visible (VIS) and near-infrared (NIR) channels and FIRE), we have developed absorption-line fitting routines that generate a single hierarchical physical model of components and transitions and then project that model onto the respective spectral data of each instrument, convolving to the appropriate resolution of each spectrograph. The model vector is optimized to fit all instruments simultaneously using a Markov chain Monte Carlo walker as implemented by the emcee Python package<sup>48</sup>, to determine confidence intervals from the posterior distribution. Before fitting absorption models, each spectrum was normalized by a continuum iteratively determined by cubic spline fits with outlier rejection.

For this particular absorption complex, we identified three distinct components of high-ionization gas with C IV and Si IV aligned in velocity space. The adopted Voigt profile model constrains redshifts of the C IV and Si IV components to align in velocity. As seen in Extended Data Fig. 5, the C IV component at  $z_{\text{abs}} = 5.7411$  is a marginal identification with low statistical significance. However, a firm Si IV detection is seen for all three components. Numerous low-ionization species are also present at  $z \approx 5.7$ ; these are not shown and we defer them to a later analysis, as some low-ionization transitions are blended with lower-redshift interloping absorbers.

Extended Data Table 2 lists the Voigt profile median parameters and [16%, 84%] confidence intervals on the fit. It should be noted that XShooter and FIRE probably do not resolve fine velocity structures, so the Doppler parameters  $b$  in the fits may represent a velocity dispersion among components that would be separated at higher resolution, rather than the intrinsic width of a single component. However, tests indicate that the total column densities of these fits are robust when interpreted as a sum of the unresolved blend.

## HST broadband imaging

In the field of QSO J1030+0524, we carried out HST broadband imaging in the F775W (mean wavelength  $\lambda_{\text{mean}} = 7,731$  Å) and F160W ( $\lambda_{\text{mean}} = 15,436$  Å) bands (programme IDs 13303 and 15085). In the HST archival database, further observations (programme ID 9777) in F775W and F850LP ( $\lambda_{\text{mean}} = 9,080$  Å) are available. All the HST images were processed and co-added using the DrizzlePac software<sup>49</sup>.

These images were used to search for rest-frame UV counterparts of the claimed [C II] emitters. For sources at  $z \approx 5.7$ , the F775W, F850LP and F160W bands sample the rest-frame 1,150 Å (including the wavelength of Ly $\alpha$ ), 1,350 Å and 2,300 Å, respectively. The 3'' × 3'' cutout images are shown in Extended Data Fig. 6. No notable counterpart was found at the positions of the [C II] sources, yielding  $2\sigma$  upper limits of 45 nJy (F775W), 59 nJy (F850LP) and 31 nJy (F160W) for the aperture photometry in 0.7'' diameter. Here the standard deviation of the photometric flux is estimated by conducting aperture photometry at random sky positions.

The rest-frame FUV flux traces unobscured star formation of a galaxy. We converted the F850LP fluxes to the UV-based  $\text{SFR}_{\text{UV}}$  adopting a relation ( $\text{SFR}_{\text{FUV}} (M_\odot \text{ year}^{-1}) = 0.72 \times 10^{-28} L_\nu (\text{erg s}^{-1} \text{ Hz}^{-1})$ )<sup>40</sup>, yielding  $\text{SFR}_{\text{UV}} < 2.4 M_\odot \text{ year}^{-1}$ .

## MUSE observation

We retrieved the archival data of the integral field spectroscopy in this field taken with the MUSE on the VLT UT4 under ESO programme

095.A-0714(A). The datacube covers a  $1' \times 1'$  region centred at the position of QSO J1030+0524 across the wavelength range 4,750–9,350 Å with the total on-source exposure time of 6.4 h. The observations were carried out in the WFM-NOAO-N mode in excellent seeing. The spatial FWHM is  $\approx 0.6''$  measured on the ‘white-light’ image, constructed from collapsing the reduced datacube over the full wavelength range.

The initial data reduction was carried out with the MUSE pipeline (v2.8.5; ref. 50). With the pipeline, we applied bias subtraction, flat fielding, wavelength calibration and produced datacubes and pixel tables. The quality of the sky subtraction in the pipeline reduced version is limited by flat-fielding errors, owing to temperature fluctuations in the instrument. As a post-processing step, we apply CubEx (see, for example, refs. 51,52) to perform self-calibration to improve the flat fielding and sky subtraction. MUSE datacubes often contain small shifts ( $< 2''$ ) in the field centre with respect to the astrometry solution in the header, which is caused by the so-called ‘derotator wobble’<sup>53</sup>. To facilitate matched spectroscopy for the ALMA detections in MUSE, it was essential that the astrometry be well calibrated. The MUSE field of view does not contain any stars with Gaia astrometry, so instead we used the HST Advanced Camera for Surveys F775W image as a bridge to propagate Gaia astrometry to the MUSE data.

We used the MUSE datacube to search for counterparts of [C II]1030Å and B in the Ly $\alpha$  emission line within search radii of approximately 3'', or 20 pkpc, in position and  $\pm 500$  km s $^{-1}$  in velocity. No notable Ly $\alpha$  emission was detected at the expected positions and wavelengths for these [C II] sources, yielding a  $2\sigma$  upper limit of approximately  $1 \times 10^{-18}$  erg s $^{-1}$  cm $^{-2}$  on the observed Ly $\alpha$  fluxes.

## Data availability

The ALMA, HST and VLT datasets used in this work are publicly available, respectively, through the ALMA data archive at <https://almascience.nao.ac.jp/aq/> (project code 2017.1.00621.S), the HST data archive at <https://archive.stsci.edu/missions-and-data/hst> (proposal IDs 9777, 13303 and 15085) and the European Southern Observatory Science Archive at <http://archive.eso.org> (programme IDs 084.A-0360, 086.A-0162, 086.A-0574, 087.A-0607 and 095.A-0714).

## Code availability

The ALMA data were processed using the CASA pipeline version 5.4, which is available at <https://casa.nrao.edu>. The Interferopy package that includes the findclumps source finding program is available at <https://github.com/interferopy/interferopy>. The VLT/XShooter spectral data were reduced using the Pypeit package available at <https://github.com/pypeit/Pypeit>. The Magellan FIRE spectral data were reduced using the FIREHOSE pipeline available at <https://wikis.mit.edu/confluence/display/FIRE/FIRE+Data+Reduction> and corrected using the xtellcor package available at <http://irtfweb.ifa.hawaii.edu/~spex/index.html>. The DrizzlePac software used for the HST data reduction is available at <https://www.stsci.edu/scientific-community/software/drizzpac.html>. The reduction pipelines of the VLT instruments are available at <https://www.eso.org/sci/software/pipelines/>.

32. Planck Collaboration et al. Planck 2018 results. VI. Cosmological parameters. *Astron. Astrophys.* **641**, A6 (2020).

33. Alam, S. et al. The eleventh and twelfth data releases of the Sloan Digital Sky Survey: final data from SDSS-III. *Astrophys. J. Suppl.* **219**, 12 (2015).
34. McMullin, J. P., Waters, B., Schiebel, D., Young, W. & Golap, K. in *Astronomical Data Analysis Software and Systems XVI ASP Conference Series Vol. 376* (eds Shaw, R. A., Hill, F. & Bell, D. J.) 127 (Astronomical Society of the Pacific, 2007).
35. Walter, F. et al. ALMA spectroscopic survey in the Hubble Ultra Deep Field: survey description. *Astrophys. J.* **833**, 67 (2016).
36. Boogaard, L., Meyer, R. A. & Novak, M. Interferopy: analysing datacubes from radio-to-submm observations. *Zenodo* <https://zenodo.org/record/5775604> (2021).
37. Popping, G. et al. Sub-mm emission line deep fields: CO and [C II] luminosity functions out to  $z = 6$ . *Mon. Not. R. Astron. Soc.* **461**, 93–110 (2016).
38. Ferrara, A. et al. The ALMA REBELS Survey. Epoch of Reionization giants: properties of dusty galaxies at  $z = 7$ . *Mon. Not. R. Astron. Soc.* **512**, 58–72 (2022).
39. Béthermin, M. et al. The ALPINE-ALMA [CII] survey: data processing, catalogs, and statistical source properties. *Astron. Astrophys.* **643**, A2 (2020).
40. Madau, P. & Dickinson, M. Cosmic star-formation history. *Annu. Rev. Astron. Astrophys.* **52**, 415–486 (2014).
41. Chabrier, G. Galactic stellar and substellar initial mass function. *Publ. Astron. Soc. Pac.* **115**, 763–795 (2003).
42. Vernet, J. et al. X-shooter, the new wide band intermediate resolution spectrograph at the ESO Very Large Telescope. *Astron. Astrophys.* **536**, A105 (2011).
43. Simcoe, R. A. et al. FIRE: a facility class near-infrared echelle spectrometer for the Magellan telescopes. *Publ. Astron. Soc. Pac.* **125**, 270 (2013).
44. Prochaska, J. et al. Pypeit: the Python spectroscopic data reduction pipeline. *J. Open Source Softw.* **5**, 2308 (2020).
45. Gagné, J., Lambides, E., Faherty, J. K. & Simcoe, R. FireHose\_v2: Firehose v2.0. *Zenodo* <https://zenodo.org/record/18775> (2015).
46. Vacca, W. D., Cushing, M. C. & Rayner, J. T. A method of correcting near-infrared spectra for telluric absorption. *Publ. Astron. Soc. Pac.* **115**, 389–409 (2003).
47. Cushing, M. C., Vacca, W. D. & Rayner, J. T. Spextool: a spectral extraction package for SpeX, a 0.8–5.5 micron cross-dispersed spectrograph. *Publ. Astron. Soc. Pac.* **116**, 362–376 (2004).
48. Foreman-Mackey, D., Hogg, D. W., Lang, D. & Goodman, J. emcee: the MCMC hammer. *Publ. Astron. Soc. Pac.* **125**, 306–312 (2013).
49. Hoffmann, S. L. et al. The DrizzlePac Handbook, Version 2.0. Space Telescope Science Institute <https://hst-docs.stsci.edu/drizzpac> (2021).
50. Weilbacher, P. M. et al. The data processing pipeline for the MUSE instrument. *Astron. Astrophys.* **641**, A28 (2020).
51. Borisova, E. et al. Ubiquitous giant Ly $\alpha$  nebulae around the brightest quasars at  $z < 3.5$  revealed with MUSE. *Astrophys. J.* **831**, 39 (2016).
52. Cantalupo, S. et al. The large- and small-scale properties of the intergalactic gas in the Slug Ly $\alpha$  nebula revealed by MUSE He II emission observations. *Mon. Not. R. Astron. Soc.* **483**, 5188–5204 (2019).
53. Bacon, R. et al. The MUSE 3D view of the Hubble Deep Field South. *Astron. Astrophys.* **575**, A75 (2015).

**Acknowledgements** This work is based on the ALMA observation under ADS/JAO.

ALMA#2011.0.01234.S. ALMA is a partnership of the ESO (representing its member states), NSF (USA) and NINS (Japan), together with NRC (Canada), MOST and ASIAA (Taiwan) and KASI (Republic of Korea), in cooperation with the Republic of Chile. The Joint ALMA Observatory is operated by the ESO, AUI/NRAO and NAOJ. This research makes use of observations made with the NASA/ESA HST obtained from the Space Telescope Science Institute, which is operated by the Association of Universities for Research in Astronomy, Inc., under NASA contract NAS 5-26555. This paper includes data gathered with the 6.5-m Magellan telescopes located at Las Campanas Observatory, Chile. Data analysis was in part carried out on the Multi-wavelength Data Analysis System operated by the Astronomy Data Center, NAOJ. We acknowledge support from JSPS KAKENHI grant number JP21K13956.

**Author contributions** D.K., S.J.L., R.B. and R.A.S. discussed and planned the ALMA programme and the HST observations in the F775W band. R.A.S. obtained the HST observation in the F160W band. A.-C.E. and R.A.S. analysed the XShooter and FIRE spectroscopic data of QSO J1030+0524. R.M. reduced and calibrated the MUSE data. S.J.L., J.M., R.A.S., R.M. and A.-C.E. contributed to the discussion of the presented results and the preparation of the manuscript. D.K. led the team, being principal investigator of the ALMA programme, analysed the ALMA and ancillary data, wrote the main text and the Methods section, and produced all figures and the table in the article.

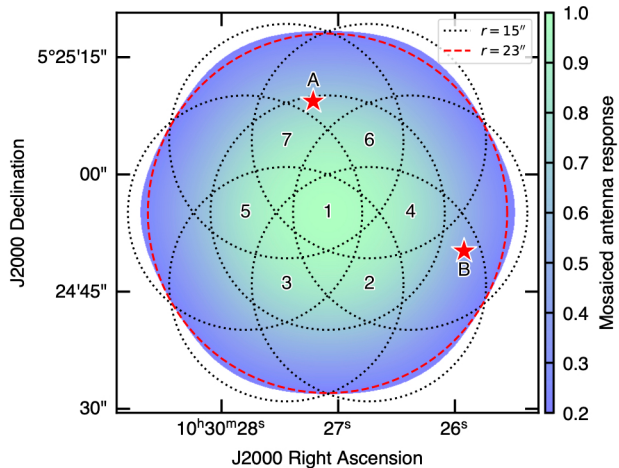
**Competing interests** The authors declare no competing interests.

**Additional information**

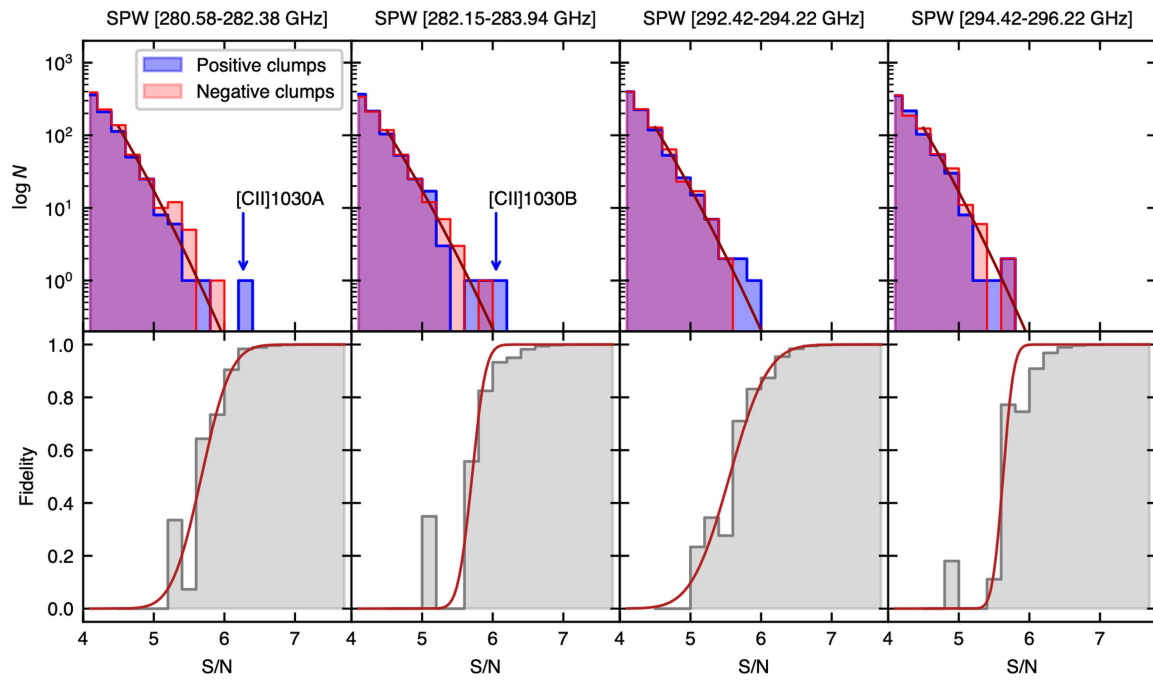
**Correspondence and requests for materials** should be addressed to Daichi Kashino.

**Peer review information** *Nature* thanks the anonymous reviewers for their contribution to the peer review of this work.

**Reprints and permissions information** is available at <http://www.nature.com/reprints>.


**Extended Data Fig. 1 | Antenna response (primary beam) map of the mosaic**

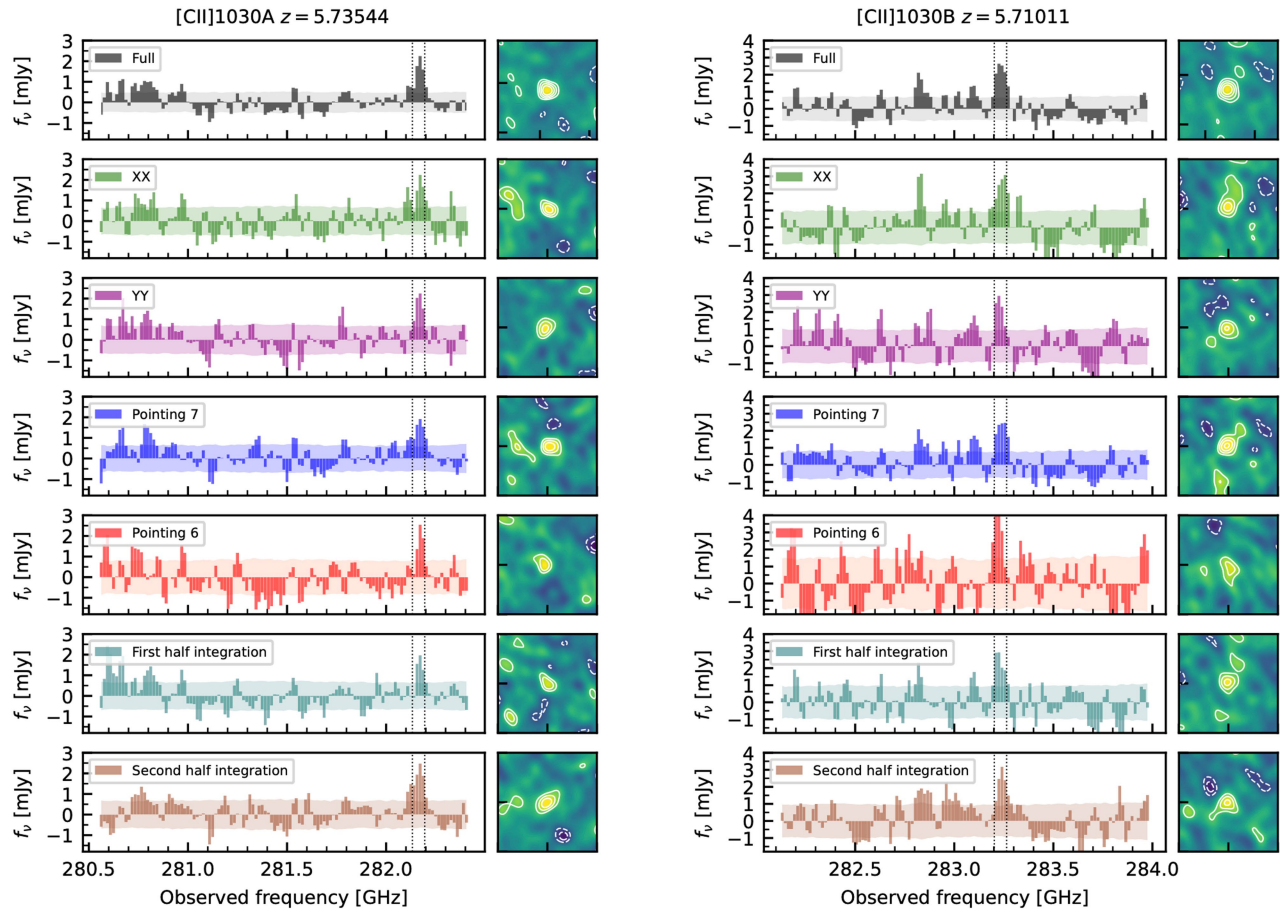
**ALMA observation.** The response is normalized to one at the field centre and the survey field is defined as the area of about  $23''$  in radius at which the relative response is above 20%. The primary beam size of the seven individual pointings ( $r = 15''$ ) that compose the mosaic observation is shown by the dotted-line circles with pointing numbers from 1 to 7. The positions of the two [C II] sources ([C II]1030A and B) are marked by red stars.



**Extended Data Fig. 2 | Fidelity in our line search.** Upper panels, number of positive (blue) and negative (that is, noise; red) peaks detected in the four ALMA datacubes (one column for each). The frequency range of each SPW is

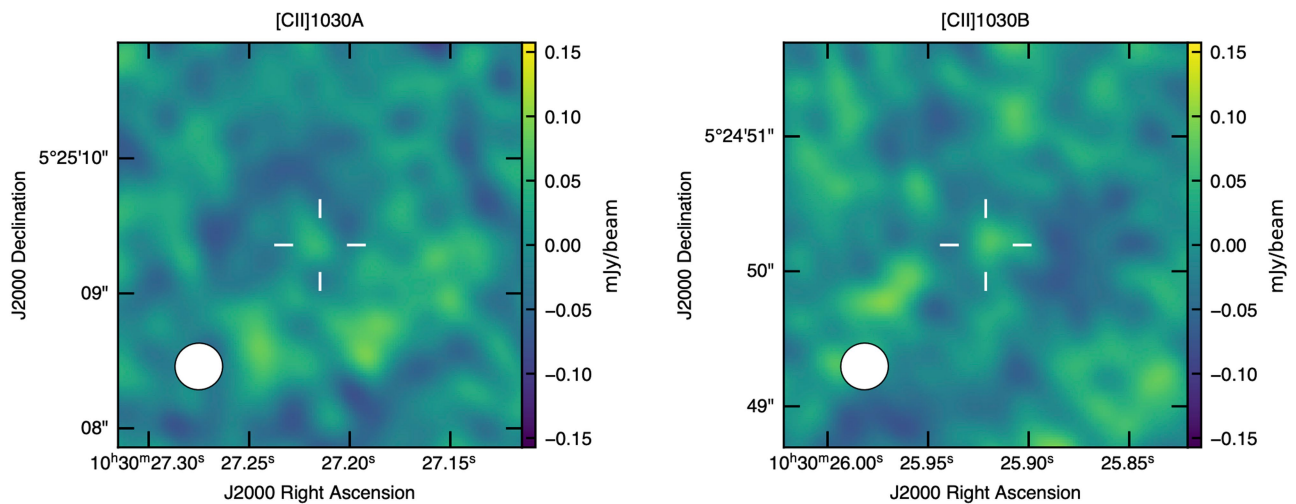
denoted at the top. Lower panels, the fidelity at given S/N with the model fit as an error function (solid red line).

# Article

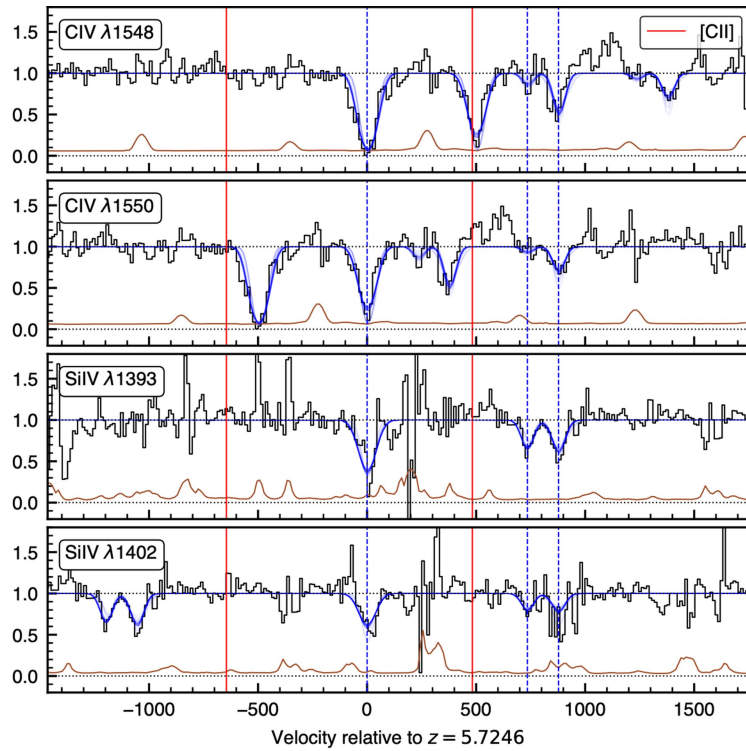


**Extended Data Fig. 3 | Reliability check of the [C II] detection.** For each of [C II]1030A (left) and B (right), the spectra and the [C II] moment-0 maps ( $2'' \times 2''$ ) constructed in the reliability tests are compared with those from the full dataset that are shown in the top row. The second and third rows show the results under only XX or YY polarization. The fourth and fifth rows show the results for the first and second half exposure time intervals. The sixth and seventh rows show

the results from processing each of the two individual ALMA pointings that cover the source position. In the spectral plots, the collapsed channel window is shown by dotted vertical lines. In the [C II] intensity maps, the solid (dashed) contours mark positive (negative) steps of  $1\sigma$  root mean square starting at  $2\sigma$  ( $-2\sigma$ ). All of these products from the partial dataset exhibit substantial signals that coincide both spatially and spectrally to those seen in the full dataset.

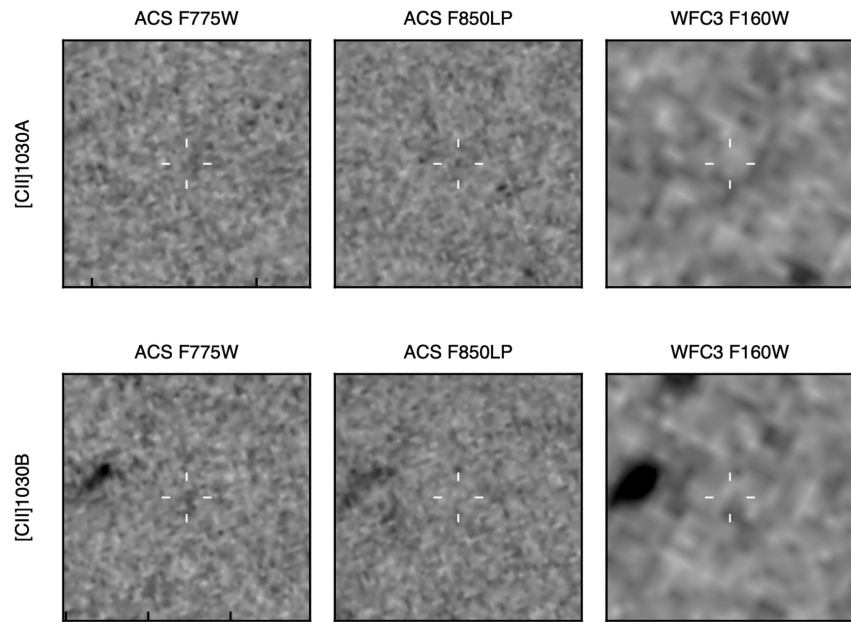


**Extended Data Fig. 4 | Continuum maps.** Each image cuts out the  $3'' \times 3''$  region centred at the position of [C II]1030A (left panel) and B (right panel). The rest-frame 1,900 GHz continuum intensity is shown by the colour scale. The synthesized continuum beam size is indicated by the white circle in the lower-left corner.



**Extended Data Fig. 5 | CIV and SiIV absorption systems at  $z_{\text{abs}} \approx 5.7$ .** Each panel corresponds to the transition labelled at the upper left. The black line shows the observed spectrum of QSO J1030+0524, whereas the light-brown line denotes the standard deviation of the flux. The blue lines indicate 50 random Voigt profiles sampled from the posterior distribution. The origin of

the velocity scale was chosen to correspond to the strongest absorption system at  $z_{\text{abs}} = 5.7246$ , which is marked along with the two other systems ( $z_{\text{abs}} = 5.7411$  and  $5.7443$ ) with the dashed blue lines. The vertical red lines indicate the relative velocities of [C II]1030A and B.



**Extended Data Fig. 6 | HST broadband images.** Each image cuts out the  $3'' \times 3''$  region centred at the position of [C II]1030A (upper row) and B (lower row). From left to right, these images are F775W, F850LP and F160W, respectively,

which sample the rest-frame 1,150 Å, 1,350 Å and 2,300 Å. No notable rest-frame UV counterpart is detected at the positions of the [C II] emission.

# Article

**Extended Data Table 1 | Expected number counts of CO sources**

Transition	Frequency (GHz)	Redshift	$\log L_{\text{CO}}$ (Jy km s <sup>-1</sup> Mpc <sup>2</sup> )	$N$
$J = 3-2$	345.80	0.22	6.46	0.02
$J = 4-3$	461.04	0.63	7.51	0.11
$J = 5-4$	576.27	1.04	8.04	0.11
$J = 6-5$	691.47	1.45	8.40	0.10
$J = 7-6$	806.65	1.85	8.66	0.05
$J = 7-6$	921.80	2.26	8.87	0.02
Total				0.40

The frequency is given in the rest frame. The redshift and luminosity are calculated under the assumption that the fainter line ( $A$ ) detected in the ALMA data is each of the CO transitions. The expected number counts of unrelated CO sources at a line flux brighter than or equal to the observed flux are provided in the fourth column.

**Extended Data Table 2 | Absorption-line measurements**

Redshift	$\log N(\text{C IV})$	$\log N(\text{Si IV})$	$b$
	(cm $^{-2}$ )	(cm $^{-2}$ )	(km s $^{-1}$ )
5.72457 [5.72455, 5.72460]	14.55 [14.52, 14.63]	13.70 [13.68, 13.72]	40.6 [35.0, 42.6]
5.74106 [5.74102, 5.74110]	13.08 [12.68, 13.20]	13.26 [13.23, 13.29]	20.8 [7.0, 22.6]
5.74426 [5.74422, 5.74428]	13.81 [13.77, 13.85]	13.31 [13.28, 13.35]	23.0 [20.6, 30.6]

The median and [16%, 84%] confidence intervals are given for each of the Voigt profile parameters. The second and third columns present the column densities of CIV and SiIV, respectively. The fourth column is the Doppler parameter  $b$  that is related to the kinetic temperature  $T$  of the gas through  $b = \sqrt{2kT/m_p}$ , in which  $k$  is the Boltzmann constant and  $m_p$  is the proton mass.